Engineering Structures 261 (2022) 114270

Contents lists available at ScienceDirect

Engineering Structures

journal homepage: www.elsevier.com/locate/engstruct

Analysis of the tension chord in the flexural response of concrete elements: Methodology and application to weft-knitted textile reinforcement

Minu Lee *, Jaime Mata-Falcón, Walter Kaufmann

Institute of Structural Engineering, Swiss Federal Institute of Technology (ETH) Zurich, Switzerland

ARTICLE INFO

Keywords:
Textile reinforced concrete
Bending
Tension chord
Experimental study
Digital image correlation
Crack behaviour
KnitCrete

ABSTRACT

The use of high-strength fibrous materials offers great potential to serve as the main reinforcement in the flexural response of lightweight concrete structures. Specifically, weft-knitted textile reinforcement allows creating complex geometries (i.e. doubly curved or folded) and introducing straight inlays as well as spatial features such as ribs within the fabric to enhance the bond conditions between the reinforcement and the concrete. While the evaluation of uniaxial tension tests to characterise the mechanical behaviour is usually straightforward, the vast majority of bending tests of textile reinforced concrete elements in the literature are limited to load–displacement data, which does not give direct information on the mechanical behaviour and makes it difficult to compare specimens with different geometries or reinforcement contents. This study presents a methodology based on digital image correlation measurements to directly assess the response in the tension chord of reinforced concrete beams in four-point bending. This methodology was applied and validated in an experimental campaign consisting of 16 bending tests with weft-knitted textile reinforcement. Various fibre materials, coating types and specimen geometries were tested, and the results were compared to corresponding uniaxial tension tests with the same type of reinforcement, generally showing a good agreement in the load-deformation behaviour and the crack kinematics. However, the textile reinforcement could not be utilised to the tensile strength obtained in uniaxial tension since all bending beams failed prematurely either in a combined bending-shear type failure (for most of the cement paste-coated textiles) or due to the delamination of the textile within a shear crack (for all epoxy-coated textiles). The Tension Chord Model with an assumed constant bond-slip relationship and an equivalent reinforcement ratio in bending yielded a good prediction of the stress–strain relationship, the tension stiffening effect, the crack widths and spacing.

1. Introduction

Textile reinforced concrete has gained much attention in both research and practice in recent years. The use of non-corrosive materials allows reducing the concrete cover to a few millimetres since the reinforcement does not have to be protected from corrosion, which leads to a drastic decrease in material consumption for the construction of new structures (e.g. [1–3]) and the strengthening of existing elements (e.g. [4–6]). Conventional textile reinforcement typically consists of a grid of orthogonally woven rovings, which are formed from multiple continuous high-strength filaments [7]. Materials used as textile reinforcement include carbon, glass or aramid fibres, which provide high strength (3000–4000 MPa) at a moderate to high stiffness (glass fibre: 70 GPa; carbon fibre: 240 GPa). Such fibres usually exhibit a linear elastic behaviour and a brittle failure mode without any ductility, which leads to large scatter of the material properties and high sensitivity to secondary forces and lateral loading, considerably reducing the strength of the roving compared to the individual filament [8,9]. Coating or even fully impregnating the rovings can substantially improve the mechanical performance by enhancing their resistance against abrasion [10,11], the inter-fibre friction, which provides a more homogeneous stress distribution within the roving [12,13], and the bond conditions between the textile and the concrete (e.g. through sand coating) [14]. While conventional textile reinforcement is suitable for lightweight structures with flat and single curved geometries, more complex shapes (e.g. double curvature) present great challenges since the reinforcement has to be cut in many patches to fit the spatial geometry, leading to problems with the directionality of the grid and many unwanted lap splices.

* Corresponding author.
E-mail addresses: mlee@ethz.ch, lee@ibk.baug.ethz.ch (M. Lee).
URL: https://www.kaufmann.ibk.ethz.ch (M. Lee).

https://doi.org/10.1016/j.engstruct.2022.114270
Received 14 December 2021; Received in revised form 16 March 2022; Accepted 10 April 2022

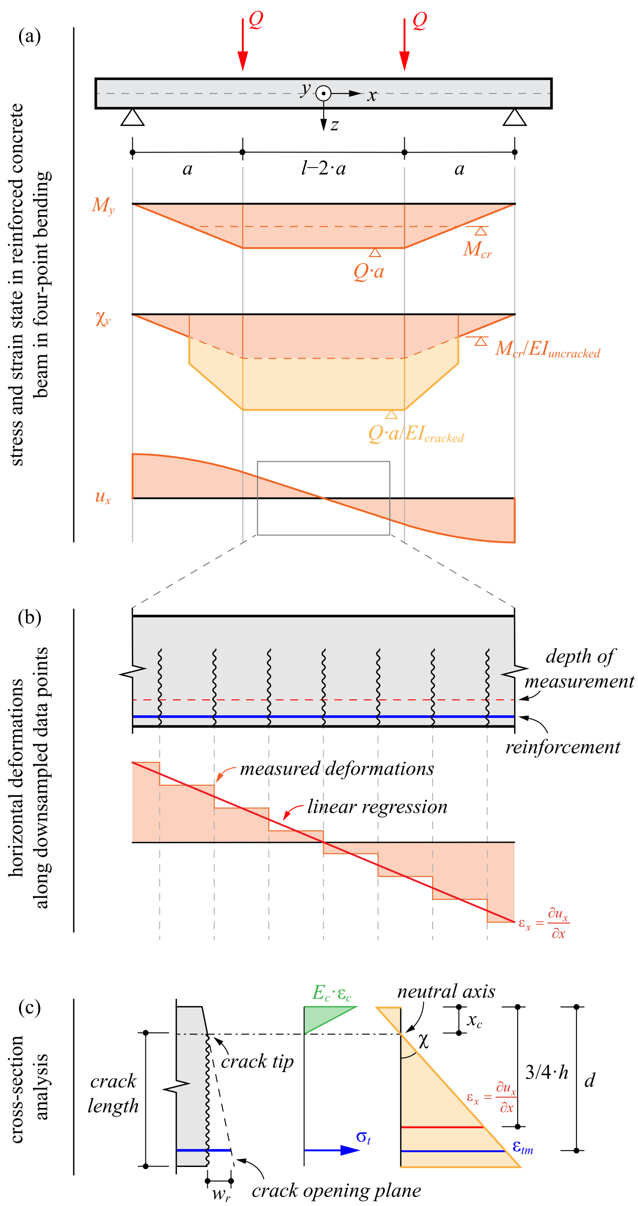

Fig. 1. Analysis of the stress and deformation state in the flexural response of reinforced concrete beams.

Weft-knitted textiles may present a solution to overcome these geometrical limitations due to the possibility of manufacturing seamless doubly curved geometries and introducing spatial features such as channels or ribs within the fabric [15]. The KnitCrete technology developed at ETH Zurich [16] is a flexible stay-in-place formwork system, which makes use of the geometric freedom of weft-knitted textiles. The fabric is tensioned in a scaffolding frame and additionally supported by cables or bending-active rods. A thin layer of either cement paste or epoxy resin is applied on the tensioned textile to increase its stiffness and strength, which is needed to withstand the loads from the fresh concrete. This construction procedure has already proved to be applicable to structures on an architectural scale, as demonstrated in the KnitCandela pavilion in Mexico City [17,18], which was realised in a collaboration between Block Research Group from ETH Zurich and Zaha Hadid Architects. However, the integration of the reinforcement remains a challenge since conventional reinforcing bars have to be bent into a complex spatial geometry, leading to less tolerance for placement. The authors revised potential approaches for reinforcement strategies in [19], concluding that using high-strength fibres as a stay-in-place textile reinforcement in the final state may significantly simplify the construction procedure and lead to efficient, lightweight concrete structures. The general behaviour of weft-knitted textile reinforced concrete was investigated in uniaxial tension [20], focusing on various knitting patterns, fibre materials, coating types and spatial features. A particular focus was given to the activation of the reinforcement and its interaction with the concrete. Compared to conventional textile reinforcement, where the grid spacing lies in the range of a few centimetres, allowing the concrete to flow around the individual rovings, weft-knitted textile reinforcement exhibits fundamentally different bond conditions due to their closed surface after coating (which follows from the small loop size, needed to serve as a stay-in-place formwork). The study in uniaxial tension [20] concluded that the integration of straight inlays into the knitted textile led to the most efficient utilisation of the fibre's strength and stiffness. While aramid rovings exhibited a beneficial post-cracking behaviour for cement paste and epoxy coating, carbon and glass fibres only achieved strain hardening when coated with epoxy resin. The poor penetration of the cement paste coating into the roving and the higher sensitivity of carbon and glass fibres to lateral loading (which led to local damages of the fibres at the crack edges) caused a premature pull-out failure shortly after cracking of the concrete.

The present study investigates the feasibility of using weft-knitted textiles as main reinforcement in flexural concrete members. A four-point bending test is a simple and reliable method to capture the structural behaviour of reinforced concrete elements subjected to uniaxial bending. While there are standardised testing procedures for textile reinforced concrete in uniaxial tension [21], the specimen geometries and reinforcement contents of bending tests found in the literature are unique to the respective study. Furthermore, the evaluation of uniaxial tension tests is straightforward and directly yields the stress–strain relationship of the textile-concrete composite. In contrast, most studies on the flexural behaviour of textile reinforced concrete characterise the structural behaviour regarding the applied loads and measured deflections, which makes it difficult to directly compare results from different studies since the results are not only dependent on the mechanical behaviour but also on the geometry. To overcome the limitations of four-point bending tests, a thorough analysis of the deformations of the tension chord is necessary to capture the mechanical performance of the reinforcement. To this end, this study presents an approach for measuring the mean strains in the tension chord of flexural members on the basis of digital image correlation (DIC) deformation measurements, which allows directly capturing distinct phenomena such as tension stiffening and comparing specimens with different geometries and reinforcement contents. While the approach is applicable for any kind of reinforcement, it is particularly suitable for textile reinforcement where the average deformations within a roving cannot be measured, not even using distributed fibre optical measurements [22] to the outside surface of a roving, due to the inhomogeneous stress distribution within the roving cross-section. The proposed procedure is then applied and validated in an experimental campaign consisting of 16 weft-knitted textile reinforced concrete members in bending. The results of the tension chord behaviour are compared to corresponding specimens in uniaxial tension, which are documented in [20]. Furthermore, the Tension Chord Model [23], originally proposed for deformed steel reinforcing bars, is adapted to the specific geometry of the weft-knitted textile reinforcement. This analytical method allows predicting the load-deformation behaviour of the flexural members with only a few material parameters that need to be known a priori.

2. Response of the tension chord in reinforced concrete beams based on digital image correlation measurements

The flexural behaviour of reinforced concrete members (referred to in the following as 'beams' regardless of their slenderness) is mainly characterised by the moment–curvature relationship of the cross-section. Although several studies on the flexural response of textile

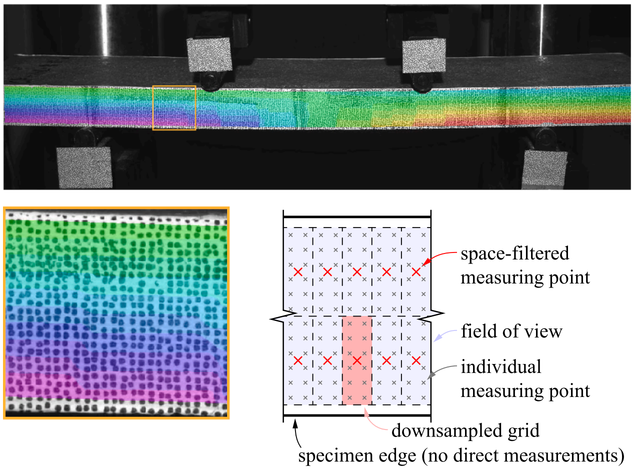

Fig. 2. Downsampling of measurement points from DIC correlation (colour plot corresponding to horizontal displacements).

reinforced concrete elements already exist (e.g. [24–27]), the experimental results are generally limited to force–displacement data, which depend on the geometric parameters of the specimens (e.g. thickness), the reinforcement type and amount, and the test setup (e.g. span). While the stresses in the reinforcement can be obtained from a cracked-elastic cross-section analysis, the back-calculation of the cross-section curvature requires several assumptions on the stiffness of cracked and uncracked areas along the beam, making it difficult to obtain reliable moment–curvature relationships and to compare the results from different tests. These issues can be avoided by directly characterising the flexural response of the tension chord in reinforced concrete beams (i.e. deformations, crack widths and crack spacings). This section presents such an approach based on digital image correlation measurements, allowing the comparison of bending tests with various specimen geometries and reinforcement contents, as well of four-point-bending and uniaxial tension tests.

Digital image correlation-based measurements allow assessing the quasi-continuous displacement field of the surface of a concrete specimen with high resolution at a low measurement uncertainty [22]. Due to the non-invasive, automated procedure, the measurements can be recorded continuously throughout the experiments without halting the load, even up to failure without endangering personnel or equipment. Moreover, the 'Automated Crack Detection and Measurement (ACDM)' tool developed at ETH Zurich [28,29] allows identifying the location of cracks and extracting their kinematics (i.e. crack opening and slip, perpendicular and parallel to the crack edge, respectively) based on DIC measurements. While ACDM directly leads to detailed information on the crack width at the height of the reinforcement and the crack spacing, the average deformations of the tension chord can be obtained following the approach described in the following.

In a four-point-bending test, the bending moment is constant between the two acting loads, allowing the analysis of the pure flexural response without any effects from shear forces. For homogeneous, linear elastic beams, the curvature of the cross-section and the longitudinal strains are directly proportional to the bending moments along the beam (Fig. 1a). The longitudinal displacements u_x can then be derived from integrating the strains ($\varepsilon_x = \partial u_x/\partial x$) over the length of the beam, which leads to a linear variation of u_x in the constant moment zone and a parabolic one in the shear spans. A reinforced concrete beam, however, cracks once the stress in the bottom fibre reaches the tensile strength, resulting in a pronounced reduction of the stiffness even if concrete and reinforcement remain elastic: typically, the cracked elastic stiffness EI^{II} is significantly smaller than the uncracked elastic stiffness EI^{I}. Due to the variable bending moment in the shear spans, the middle part of the beam is cracked (with reduced stiffness), while the regions near the supports remain uncracked. Furthermore, the interaction of the reinforcement with the surrounding concrete leads to tension stiffening in the cracked regions. Thus, the deformations of the tension chord also depend on the actual crack spacing, making it even more challenging to calculate the displacements u_x of the beam based on the applied loads and measured deflections.

Assuming linear elastic behaviour of concrete in compression and reinforcement, the depth x_c of the compression zone in the cracked section is constant, resulting in a linear moment–curvature relationship in the cracked elastic range until the reinforcement fails (for brittle materials) or starts yielding (for ductile materials). Once the crack formation is finished and a stabilised crack pattern has formed in the constant moment zone, the displacements of the concrete surface measured by digital image correlation instrumentation (DIC) can be used to assess the mean strains in the tension chord of the beam. To this end, the measured quasi-continuous displacement field is downsampled to a grid of only two rows of data points (as shown in Fig. 2), which guarantees a more stable measurement of the average deformations (attenuating local effects such as spalling or crack branching). The discrete cracks within the constant moment zone essentially cause a stepped function of the horizontal displacements u_x since the deformations of the concrete between the cracks are negligibly small. The average slope of u_x corresponds to the mean strains at the height of the downsampled measurement points (which generally does not coincide with the position of the reinforcement). It can be obtained using linear regression in the constant moment zone (solid red line in Fig. 1b).

The mean strains in the tension chord at the depth of the reinforcement can then be obtained by assuming that plane sections remain plane (in terms of mean strains). Basically, the neutral axis of the cross-section could be determined using the strain plane from the mean strains in the top and bottom rows of the downsampled data points. However, this is prone to high measurement uncertainty since the strains in the top row are close to zero. Therefore, it is preferable to determine the neutral axis using the depth of the compression zone, which can be obtained from a crack analysis. The ACDM tool allows the quasi-continuous measurement of the crack width along the crack contour, from which the crack tip can be determined. However, assessing the crack widths close to zero is again more sensitive to measurement noise and local distortions. A more robust procedure to determine the crack tip and, consequently, the compression zone depth consists in assuming linearly opening cracks, neglecting the tensile strength of the concrete, and applying linear regression on the crack widths of the bending cracks in order to estimate the crack opening plane. The average position of the neutral axis in the cracked cross-section is determined from the mean of all cracks within the constant moment zone. The mean strains (ε_{tm}) at the depth of the reinforcement (blue line in Fig. 1c) follows from the resulting curvature and strain distribution within the cross-section. This procedure allows the comparison of specimens with various geometric parameters. It also enables the analysis of the deformations at the depth of the reinforcement in specimens where the reinforcement is placed at the bottom edge of the specimen (e.g. as in stay-in-place formwork and reinforcement systems), where it is not possible to obtain direct measurements from the digital image correlation on the side face. The averaging of the DIC measuring points in the downsampling step and the application of linear regression reduces distortions in the measurements caused by outliers due to local cracking (e.g. branching or irregular crack spacing), leading to a robust measurement procedure. Furthermore, the continuous measurement of the deformations along the reinforcement allows the direct assessment of the tension stiffening effect, which usually, i.e. when only the load–deflection data is available, requires many assumptions.

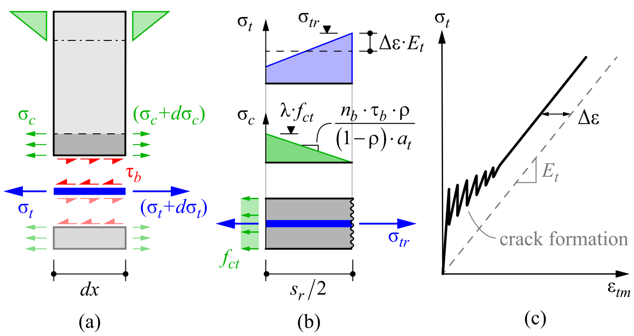

Fig. 3. Tension Chord Model in bending: (a) stress transfer between reinforcement and effective concrete area (transparent parts for specimens with concrete cover); (b) stresses of reinforcement and concrete in equivalent tension chord in one half of a cracked element; (c) reduction of mean strains ($\Delta\varepsilon$) due to tension stiffening effect in stress–strain relationship of the reinforcement.

3. Tension Chord Model for weft-knitted textile reinforced members in bending

This section presents a mechanically based model to predict the response of the tension chord in reinforced concrete beams (i.e. deformations, crack widths and crack spacings), considering the tension stiffening effect. The interaction between reinforcement and surrounding concrete reduces the mean strains compared to the bare reinforcement. At the crack, the reinforcement carries the full tensile load. Between two adjacent cracks, a part of the load is transferred to the concrete via bond shear stresses at the interface between reinforcement and concrete (Fig. 3a). The tensile stresses in the reinforcement, thus, decrease towards the centre between two cracks (Fig. 3b), consequently reducing the average strains (Fig. 3c). This effect, known as 'tension stiffening', has been extensively researched for conventional steel reinforcing bars. Specifically, the Tension Chord Model (TCM) [23] proposed a stepped, rigid-perfectly plastic bond shear stress-slip relationship to analyse the global behaviour, which significantly simplifies solving the second-order ordinary differential equation of slipping bond [30,31] since the solution is possible based on equilibrium. The authors adapted the Tension Chord Model to the specific geometry of weft-knitted textile reinforcement in uniaxial tension, obtaining good agreement with the experimental results [20] and even allowing the back-calculation of bond shear stresses. Hence, the prediction of the deformations in the tension chord following the TCM can be directly compared to the experimental results obtained from the procedure presented in Section 2 to validate the applicability of the mechanical model to weft-knitted textile reinforced concrete members in bending.

According to the TCM, tension stiffening causes a difference $\Delta\varepsilon$ between the strains of the bare reinforcement (=local strain at a crack) and the mean strain of a tension chord subjected to the same tensile force:

$$\Delta\varepsilon = \frac{\lambda \cdot f_{ct} \cdot (1-\rho_t)}{2 \cdot \rho_t \cdot E_t} \tag{1}$$

where λ = ratio of the actual crack spacing to the maximum theoretical crack spacing; f_{ct} = tensile strength of the concrete; ρ_t = geometrical reinforcement ratio; and E_t = Young's modulus of the (textile) reinforcement.

In uniaxial tension, the geometrical reinforcement ratio is usually defined as the ratio of reinforcement area to the gross concrete section. As the reinforcement content depends on the cross-sectional area of the concrete activated at its tensile strengthf_{ct}, its calculation in elements subjected to bending moments is not as straightforward. Several approaches exist in literature to estimate the effective concrete area (an overview may be found in [32,33]), but most of them depend on empirical approaches, specifically capturing the behaviour of steel reinforcing bars. Hence, they are not generally applicable for textile reinforced concrete. Marti [34] and Burns [35] presented an approach for estimating an equivalent reinforcement ratio for reinforced concrete elements in pure bending based on the Tension Chord Model. Setting the stresses in the flexural reinforcement of a rectangular cross-section subjected to the cracking moment M_{cr}, i.e.

$$\sigma_{tr0} = \frac{M_{cr}}{A_t \cdot \left(d - \frac{x}{3}\right)} = \frac{f_{ct,fl} \cdot b \cdot h^2}{6 \cdot A_t \cdot \left(d - \frac{x}{3}\right)} \tag{2}$$

equal to the stresses in the (textile) reinforcement of a tension chord at the onset of cracking

$$\sigma_{tr0} = f_{ct} \cdot \left(\frac{1}{\rho_{eq}} + n_t - 1\right) \approx \frac{f_{ct}}{\rho_{eq}} \tag{3}$$

one obtains the equivalent (textile) reinforcement ratio in bending:

$$\rho_{eq} = \frac{6 \cdot \alpha_{fl} \cdot A_t \cdot \left(d - \frac{x}{3}\right)}{h^2 \cdot b} \tag{4}$$

where σ_{tr0} = stress in the reinforcement at cracking; A_t = area of the reinforcement; d = static depth of the reinforcement; x = depth of the compression zone; h = cross-section height; b = cross-section width; $n_t = E_t/E_c$ = modular ratio; E_t, E_c = Young's moduli of (textile) reinforcement and concrete, respectively; $f_{ct,fl}$ = flexural tensile strength; $\alpha_{fl} = f_{ct}/f_{ct,fl}$ = ratio of direct to flexural tensile strength of concrete according to *fib* Model Code 2010 [36]. This formulation of the equivalent reinforcement ratio (ρ_{eq}) allows the application of the TCM in bending analogously as for pure tension.

Furthermore, the TCM allows the estimation of the crack spacing and crack widths. The maximum crack spacing (s_{r0}) depends on the bond shear stresses and the interface area between reinforcement and concrete. For weft-knitted textiles, the latter is assumed to be a plane surface (neglecting the bond ribs as spatial feature) extending over the whole width b of the specimen, which leads to

$$s_{r0} = 2 \cdot \frac{f_{ct}}{d\sigma_c/dx} = \frac{2 \cdot a_t \cdot f_{ct} \cdot \left(1-\rho_{eq}\right)}{n_b \cdot \tau_b \cdot \rho_{eq}} \tag{5}$$

where $d\sigma_c/dx$ = change in stresses of the concrete area activated in tension, as illustrated in Fig. 3b; $a_t = \frac{A_t}{b}$ = (textile) reinforcement area per unit width; n_b = number of sides of the reinforcement in contact with the concrete ($n_b = 2$ for specimens with concrete cover; $n_b = 1$ for bottom-edge reinforcement). The crack width is then obtained from

$$w_r = s_r \cdot (\varepsilon_{tm} - \varepsilon_{cm}) = \frac{\lambda \cdot s_{r0} \cdot (2 \cdot \sigma_{tr} - \lambda \cdot \sigma_{tr0})}{2 \cdot E_t} \tag{6}$$

where σ_{tr} = stress in the reinforcement at the crack, and σ_{tr0} is calculated from Equation (2). A more detailed derivation of Eqs. (5) and (6) may be found in Appendix A.

4. Experimental campaign for the validation of the evaluation methodology and mechanical model

The approaches to evaluate and predict the response of the tension chord of textile reinforced concrete members in bending proposed in Sections 2 and 3, respectively, are applied to an experimental campaign consisting of eight different configurations of textile material, coating type and specimen geometry. Two specimens were tested per configuration, resulting in 16 tests. Manufacturing and testing took place in the Structures Laboratory at ETH Zurich.

4.1. Materials and manufacturing

The dimensions of the specimens subjected to bending were as follows: width of 200 mm, length of 680 mm, and thickness of either 40 mm or 12 mm. The specimens will be referred to as beams in the

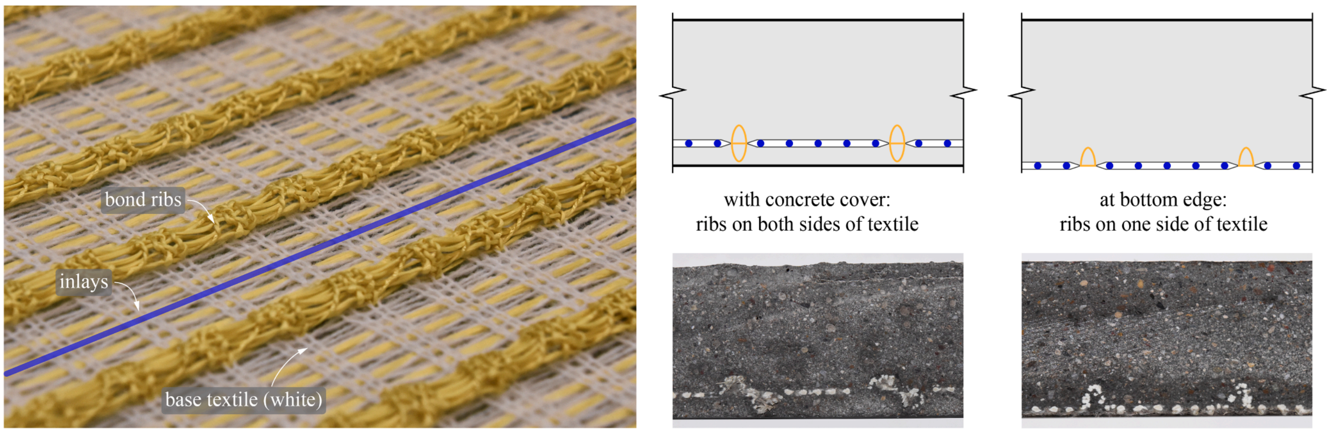

(a) (b)

Fig. 4. Weft-knitted textile reinforcement: (a) knitted textile with integrated straight inlays and spatial ribs to enhance the bond conditions; (b) placement of reinforcement within cross-section with and without concrete cover (schematic overview and cut specimen after testing). Note: blue line in (a) highlights one of the straight inlays, shown as blue circles in (b). (For interpretation of the references to colour in this figure legend, the reader is referred to the web version of this article.)

Table 1
Tensile strength and Young's modulus of textile roving (from testing [20]) and filament (notional values from manufacturer).

Inlay material	Coating	$f_{t,rov}$ [MPa]	$E_{t,rov}$ [GPa]	$f_{t,fil}$ [MPa]	$E_{t,fil}$ [GPa]
Aramid	bare/cement paste	2097	102	3000	100
	epoxy	2583	112		
Carbon fibre	epoxy	3675	224	4300	240
Glass fibre	epoxy	1960	72	2700	70

Table 2
Concrete material properties (mean ± standard deviation) from small prism tests according to EN 196–1 and tensile strength (mean) from conversion formula in *fib* Model Code 2010.

$f_{ct,fl}$ [MPa]	$f_{c,cube}$ [MPa]	E_c [GPa]	f_{ct} [MPa]
10.0 ± 0.95	83.7 ± 2.77	18.7 ± 4.45	4.4

following (due to their high slenderness, one may also refer to them as 'slab strips'). The nominal concrete cover was either 5 mm or 0 mm, i.e. for the latter, the reinforcement was placed at the bottom edge of the element. The specimens with a concrete cover were produced using the lamination process, where the coated textile reinforcement was put on the first layer of concrete and subsequently topped up with the remaining concrete. The specimens with no cover were cast upside down, i.e. the concrete was cast first, and the coated reinforcement was placed on the top surface (to prevent the concrete from flowing under the reinforcement).

4.1.1. *Textile reinforcement*

A CNC double bed knitting machine (Steiger Libra 3.130) was used for the production of the textile reinforcement. As described in [15,19,20], the knitting machine allows for various spatial features and the integration of straight inlays within the textile (as shown in Fig. 4a). The findings from [20] suggest that the use of straight inlays leads to the most efficient utilisation of the material and that spatial ribs improve the serviceability by preventing premature spalling of the concrete cover. The knitting pattern and the reinforcement content were chosen to match a series of corresponding uniaxial tension tests from a previous study of the authors [20], following Eq. (4). Three different fibre materials were used for the inlays within the textile: aramid (AF), carbon (CF) and glass (GF) fibres. The aramid and carbon fibre rovings had a fineness of 800 tex at an average spacing of 7.1 mm, whereas the glass fibres roving was 2400 tex with a spacing of 11.1 mm. The ribs, which had an approximate penetration depth into the concrete of 5 mm, were made from aramid fibres with a fineness of 160 tex on both sides of the reinforcement at an average spacing of 40 mm. In case of the specimens with no concrete cover, the ribs were only present on one face of the textile (see Fig. 4b). The base textile, which mainly served as carrier of the straight inlays, consisted of a non-structural acrylic yarn. The textiles were tensioned in a wooden frame to ensure a straight alignment of the inlays and minimise deformations during the application of the coating.

The tensile strength and Young's modulus of the inlays were determined on bare and epoxy-coated single rovings in uniaxial tension, as described in [20] (which showed that bare and cement-paste coated rovings exhibited similar strength and stiffness). The material parameters from the tests and the notional filament strength and stiffness are summarised in Table 1.

4.1.2. *Coating*

There were two different types of coating materials. A low-viscous two-component epoxy resin [37], specifically developed for the lamination and impregnation of textile fibres, was used for all inlay materials (aramid, carbon and glass fibres). The initial applications of KnitCrete made use of a highly fluid cement paste consisting of a blended ordinary Portland cement, a polycarboxylate ether based superplasticiser and stabilising nanoparticles (mix design courtesy of Dr. Lex Reiter, Chair of Physical Chemistry of Building Materials at ETH Zurich) [16]. The results from [20] showed that carbon and glass fibres with cement paste coating prematurely failed shortly after cracking of the concrete, either in a brittle manner or with a pronounced softening behaviour due to pull-out of the inner fibre core from the roving. Therefore, the cement paste coating was only applied on configurations with aramid inlays.

Both types of coatings were manually applied using paint brushes. Only the inlays were coated, and the spatial ribs remained uncoated to allow the concrete to penetrate the void created by the rib, thereby enhancing the mechanical interlock between textile and matrix. The cement paste coated textiles were left in a climate chamber (20 °C and 90% relative humidity) for three days before casting. The epoxy coating was cured for at least 24 h at room temperature.

4.1.3. *Concrete*

The concrete was mixed in the laboratory. It consisted of sand with a maximum aggregate size of 2 mm (1368 kg/m^3), Portland cement CEM I (616 kg/m^3), micro-silica (53.6 kg/m^3) and superplasticiser (2.91 kg/

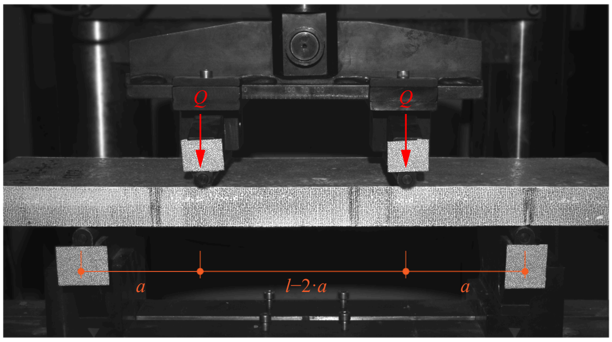

Fig. 5. Weft-knitted textile reinforced concrete beams tested in four-point bending test.

m^3) at a water-to-cement ratio of 0.41. The specimens were cast in a wooden formwork, as outlined at the beginning of Section 4.1. The concrete was compacted on a shaking table. The vibration was maintained while placing the reinforcement to minimise air voids at the interface between textile and concrete. The specimens were left to harden in a climate chamber for 10 days before testing.

The material properties were determined according to EN 196-1 [38]: The flexural tensile strength ($f_{ct,fl}$) was obtained from three-point bending tests on small prisms (40 mm × 40 mm × 160 mm) and the cube compressive strength ($f_{c,cube}$) from the resulting two halves of each prism. The uniaxial tensile strength was estimated from the measured flexural tensile strength using the conversion formula in *fib* Model Code 2010 [36]. Table 2 summarises the results from the material tests. The concrete was mixed in 5 batches, whereby 3 prisms were made for each batch.

4.2. Specimens and test setup

All textile-reinforced concrete beams were tested in four-point-bending in a Walter + Bai 100 kN universal testing machine in the Structures Laboratory at ETH Zurich (Fig. 5). The total span was between 440 mm and 500 mm. The shear span varied between 120 mm and 215 mm, leading to various ratios of shear span to static depth of the beam (a/d=shear slenderness). Table 3 summarises all tested specimens with their reinforcement layout and geometrical parameters. There were two identical specimens ('twins') per configuration of fibre material and coating type. In the cases of the textiles with aramid inlays, the specimens with and without concrete cover are denoted as 'c5′ and 'c0′, respectively. The configurations with increased shear slenderness are denoted with an asterisk (*).

The supports and the load introduction consisted of cylindrical rollers, which allowed the free rotation and horizontal elongation of each specimen. The tests were run with a controlled displacement rate of the hydraulic actuator, which was adjusted during the test as follows:

_ Before cracking: 0.2 mm/min
_ During crack formation: 0.5 mm/min
_ After full crack formation: 1.0 mm/min

4.3. Instrumentation

The force measurement was directly taken from the load cell of the testing machine. The application of 3D-digital image correlation allowed measuring a quasi-continuous displacement field over the surface of the concrete beam. A pair of FLIR Grasshopper®3 cameras (4096 × 3000 px) with a focal length of 25 mm (Linos MeVis-C) at a stereo angle of approximately 25° yielded an average resolution of 7.0 px/mm (for the given field of view with a width of ca. 585 mm). The correlation was performed with the commercial software 'VIC-3D' (Correlated Solutions Inc. [39]). A randomly speckled pattern with a speckle size of 0.7 mm was applied onto the white-painted specimen surface to guarantee maximum contrast, thus improving the correlation. The zero displacement test performed according to [40] and [22] resulted in an average noise level of $\sigma(U,V) = 5{\cdot}10^{-4}$mm and$\sigma(\varepsilon_1,\varepsilon_2) = 70\,\mu\varepsilon$, using the following correlation parameters: subset size = 19 px, step size = 5 px and strain filter size = 9.

The crack kinematics were determined on the basis of the digital image correlation measurements. The results from the quasi-continuous displacement and strain field were analysed in the open-source software 'Automated Crack Detection and Measurement (ACDM)' [28,29] to obtain and evaluate the crack pattern and the crack widths. Since the field of view of the digital image correlation measurements did not contain the edges of the specimens, the crack width of the textiles without cover was estimated from the measured crack widths assuming linearly opening cracks.

5. Experimental results and model validation

For the assessment of the mean strains of the reinforcement, the procedure described in Section 2 was applied to all specimens. Fig. 6 shows the vertical displacements and the horizontal elongation within the constant moment zone at different load stages of Specimen 'AF-C-c0-1′, which shows that the cracks dominated the deformations of the tension chord. The mean strains were determined at every time step of the experiment. The analysis of the crack kinematics in Fig. 7 shows the measured crack openings over their length of a selection of cracks within

Table 3
Specimen configuration of bending beams with various fibre materials, coating types and specimen geometries.

Specimen	Fibre material	Coating	No. of inlays [–]	A_t [mm^2]	ρ_{eq} [%]	b [mm]	h [mm]	d [mm]	a [mm]	l [mm]	a/d [–]
AF-C-c0	Aramid	Cement paste	30	16.7	0.53	200.7	39.8	39.4	120	440	3.0
			30	16.7	0.52	200.9	40.3	39.9			
AF-C-c5			29	16.1	0.43	201.0	39.5	32.7	120	440	3.7
			29	16.1	0.43	200.7	39.6	32.9			
AF-E-c0		Epoxy	30	16.7	0.53	201.4	39.7	39.3	140	500	3.6
			30	16.7	0.53	201.1	39.9	39.5			
AF-E-c5			28	15.6	0.43	201.0	39.4	33.9	120	440	3.5
			28	15.6	0.44	200.4	39.2	34.2			
CF-E-c5	Carbon fibre	Epoxy	28	12.7	0.36	201.3	39.6	34.8	120	440	3.5
			28	12.7	0.34	201.0	39.1	32.7			
GF-E-c5	Glass fibre	Epoxy	19	17.9	0.49	200.8	39.6	33.7			
			19	17.9	0.49	201.2	39.9	34.3			
AF-E-c5*	Aramid	Epoxy	29	16.1	0.43	201.2	40.1	34.1	215	500	6.0
			29	16.1	0.41	201.6	40.8	33.8			
AF-E-c0*			30	16.7	1.51	201.4	12.3	11.9	140	500	12.0
			30	16.7	1.61	202.5	11.3	10.9			

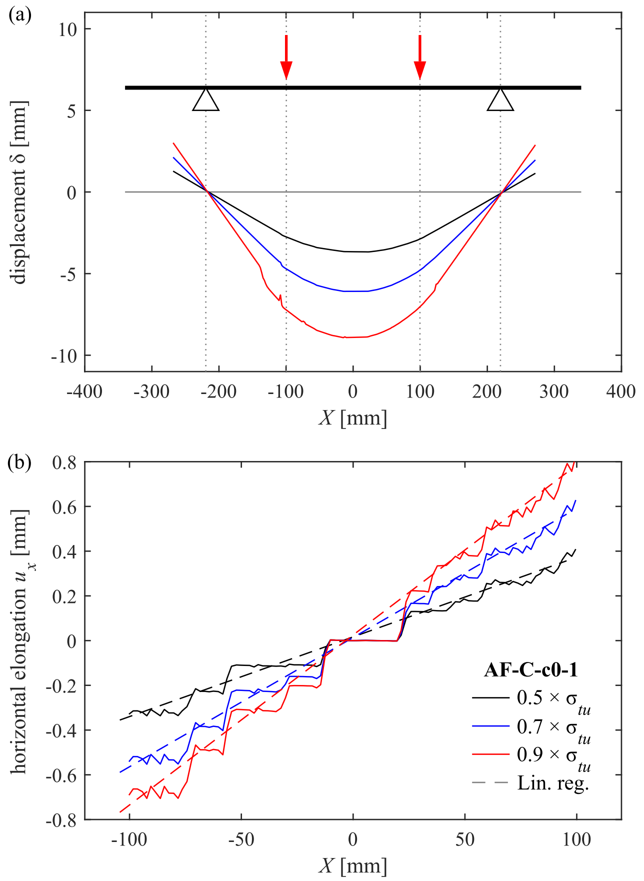

Fig. 6. Deformations of Specimen ‘AF-C-c0-1′ at various load levels: (a) vertical displacement; (b) elongation of tension chord in constant moment zone.

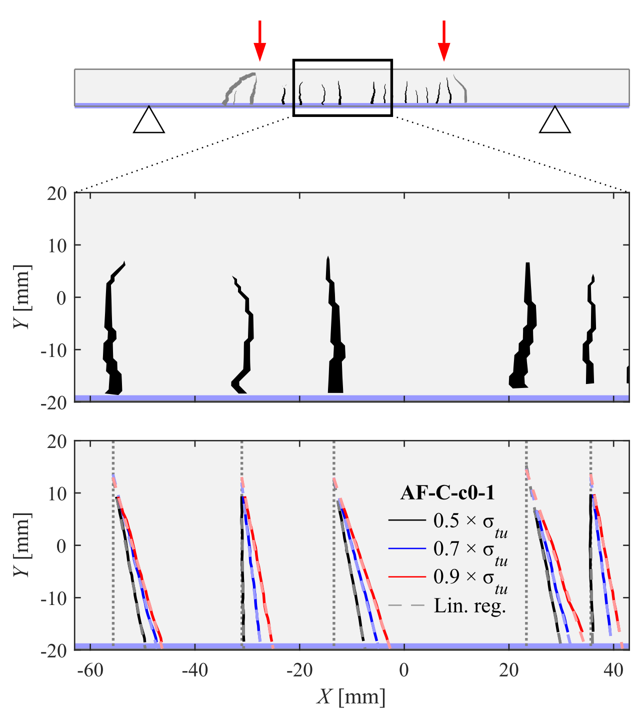

Fig. 7. Analysis of crack kinematics in constant moment zone of Specimen ‘AF-C-c0-1′ at various load levels.

the constant moment zone at various load levels as solid lines. Note that no direct measurements were possible at the bottom edge of the specimen (i.e. height of the reinforcement), as explained in Section 2, and crack openings in the upper quarter of the cross-section were not considered to avoid any distortion of the measurements due to peculiar effects such as crack branching. The crack opening planes obtained from linear regression (light dashed lines) correspond well to the measured crack widths, as graphically illustrated in Fig. 7 and statistically analysed in Fig. 13 in Appendix A. Therefore, the assumed extrapolation of the crack opening at the bottom edge of the specimen is reasonable.

5.1. General load-deformation behaviour

Fig. 8 shows the load-deformation behaviour of the weft-knitted textile reinforced concrete beams with concrete cover (denoted as ‘c5′ and shown as solid lines) and without concrete cover (i.e. at the bottom edge of the specimen, denoted as ‘c0′ and shown as dashed lines). The corresponding reference tests in uniaxial tension with the same type of inlay fibre material containing the same amount of reinforcement are displayed as dotted lines. The deflection was taken at mid-span, and the bending moment was obtained from the applied load of the testing machine and the respective spans of the specimens. The tensile force in the textile reinforcement at the cracks within the constant moment zone was determined from a cross-sectional analysis assuming a linear distribution of concrete stresses and the average compression zone height determined from the crack analysis, as outlined in Section 2. The textile stresses (σ_t) were then calculated by dividing the force in the tension chord by the nominal cross-sectional area of the inlays:

$$\sigma_t = \frac{Q \cdot a}{\left(d - \frac{x}{3}\right) \cdot A_t} \tag{7}$$

Following the findings from the corresponding uniaxial tension tests [20], the contributions from the non-structural yarn in the base textile and the bond ribs made from aramid were neglected.

The general behaviour of most specimens followed the typical response known from conventional textile reinforcement [8,9], which also met the expectations from the findings of the corresponding uniaxial tension tests [20]. In the initial uncracked state, the behaviour was governed by the concrete stiffness. Once the specimens reached their tensile strength in the weakest section, multiple distributed cracks formed consecutively within the constant moment zone. After most cracks had formed and the crack pattern had stabilised, the concrete beams exhibited a fairly linear increase of deformation with increasing load, which is visible in both the moment-deflection (Fig. 8a) and stress–strain relationships (Fig. 8b). No or just few further cracks formed in the constant moment zone during this phase, while the existing cracks widened with increasing deformation (see also Section 5.2). With further increase of the load, more bending cracks formed in the shear spans since more regions exceeded the cracking moment.

The stiffness of the reinforcement in the post-cracking phase generally corresponded well with the results from the roving tests (denoted as grey lines in the stress–strain relationship). Only the specimens with cement paste-coated aramid fibres and concrete cover (‘AF-C-c5′) displayed a stiffer behaviour in the initial phase after cracking, which seemed to decrease towards failure. The effect of tension stiffening was visible in all specimens as the mean strains at a given stress level were clearly smaller than those expected in the bare textile. The bending beams with concrete cover showed a good agreement with the corresponding uniaxial tension tests. The beams with bottom-edge reinforcement (with no cover) seemed to display a slightly smaller tension stiffening effect. This is due to the fact that the effective concrete area contributing to the load transfer between the cracks is smaller in these specimens since the interface between reinforcement and concrete amounts to only half of the area of the specimens with concrete cover. The only exception to the reduced tension stiffening was one of the

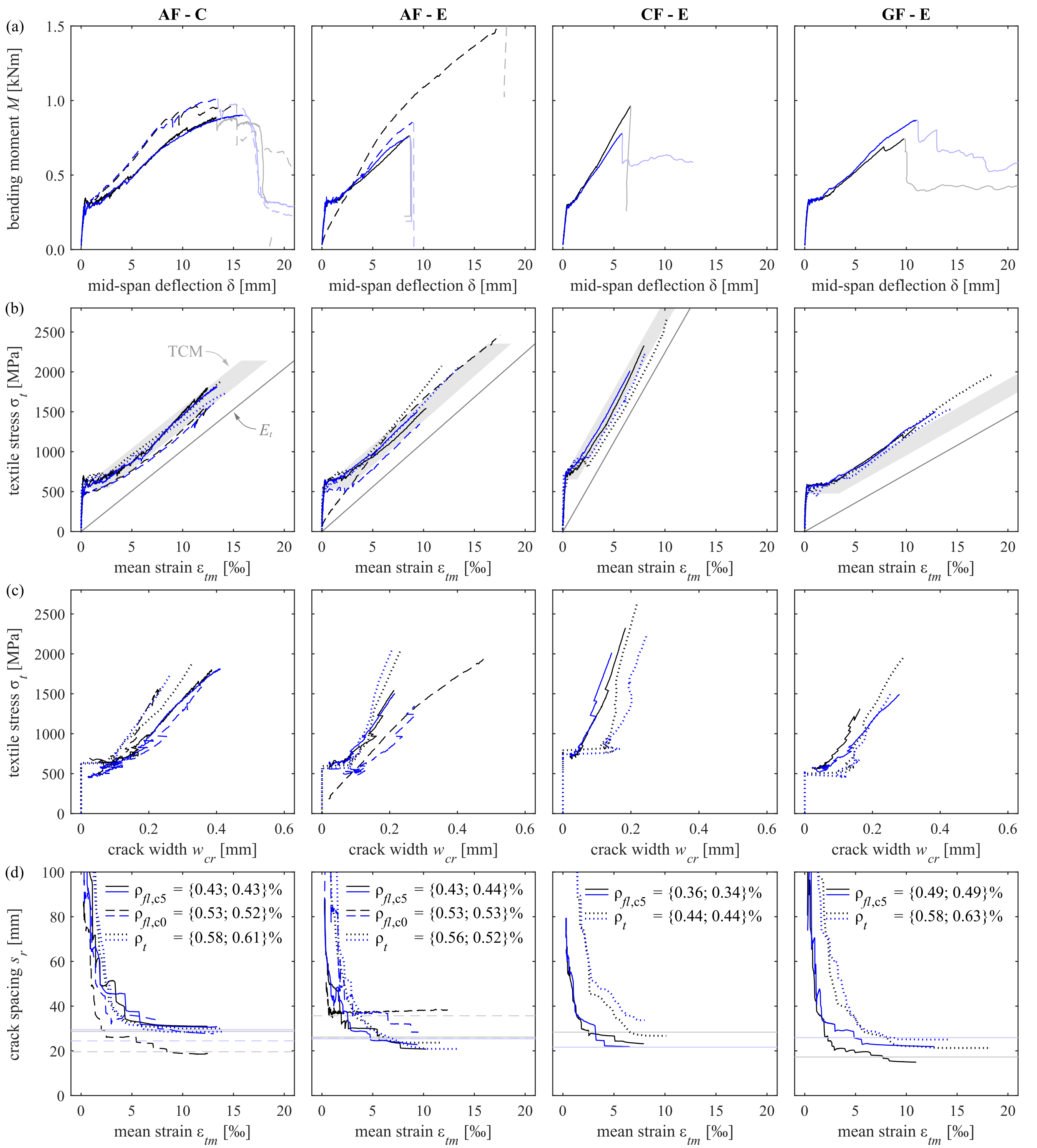

Fig. 8. Load-deformation and crack behaviour of beams with concrete cover (denoted as 'c5' and shown as solid lines) and without concrete cover (denoted as 'c0' and shown as dashed lines), and uniaxial tension ties (denoted as '*t*' and shown as dotted lines): (a) moment vs. deflection; (b) textile stresses vs. mean strains in the tension chord and tie, respectively (grey area: prediction following the TCM); (c) textile stresses vs. average crack width within constant moment zone and tension tie; (d) crack spacing vs. mean strains.

specimens with aramid inlays, epoxy coating and no concrete cover (black dashed line in 'AF-E'). Due to problems with the measurement setup, this specimen had to be unloaded and re-loaded, and only the data from the second loading cycle could be recorded. Therefore, the specimen was initially already fully cracked. Once the load exceeded the cracking load, the behaviour of the beam was expected to be the same as in the other specimens. However, the bending moment and consequently the textile stresses at ultimate load were considerably higher compared to the corresponding twin experiment and the uniaxial tension tests. The initial stiffness was higher in both the load–deflection behaviour and the stress–strain relationship, and the tension stiffening effect was larger than in its twin, as well as the corresponding bending beams with concrete cover. A possible explanation for this different behaviour will be discussed based on the observed crack kinematics in

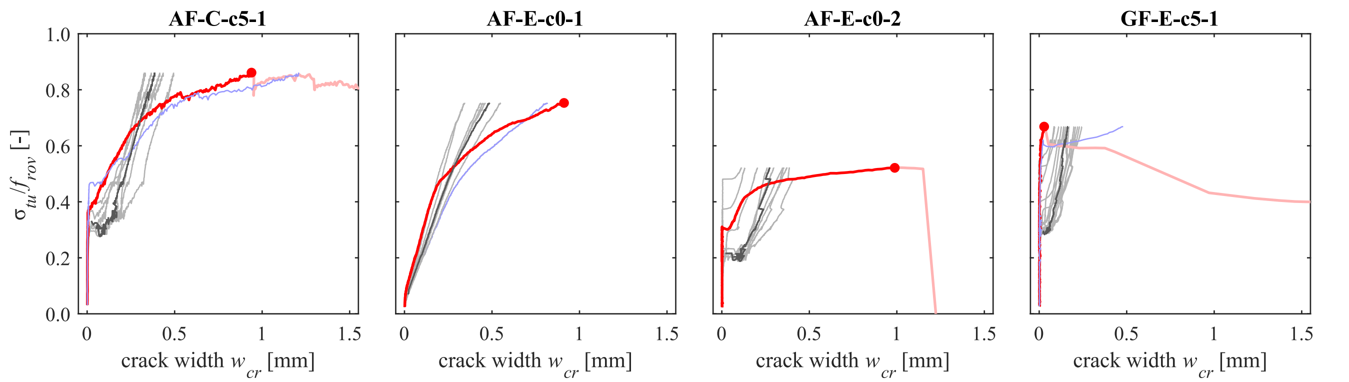

Fig. 9. Crack openings of all cracks (grey: bending cracks within constant moment zone; black: average crack width; red: governing failure crack, ultimate load reached at the circle; blue: secondary major crack in shear span). (For interpretation of the references to colour in this figure legend, the reader is referred to the web version of this article.)

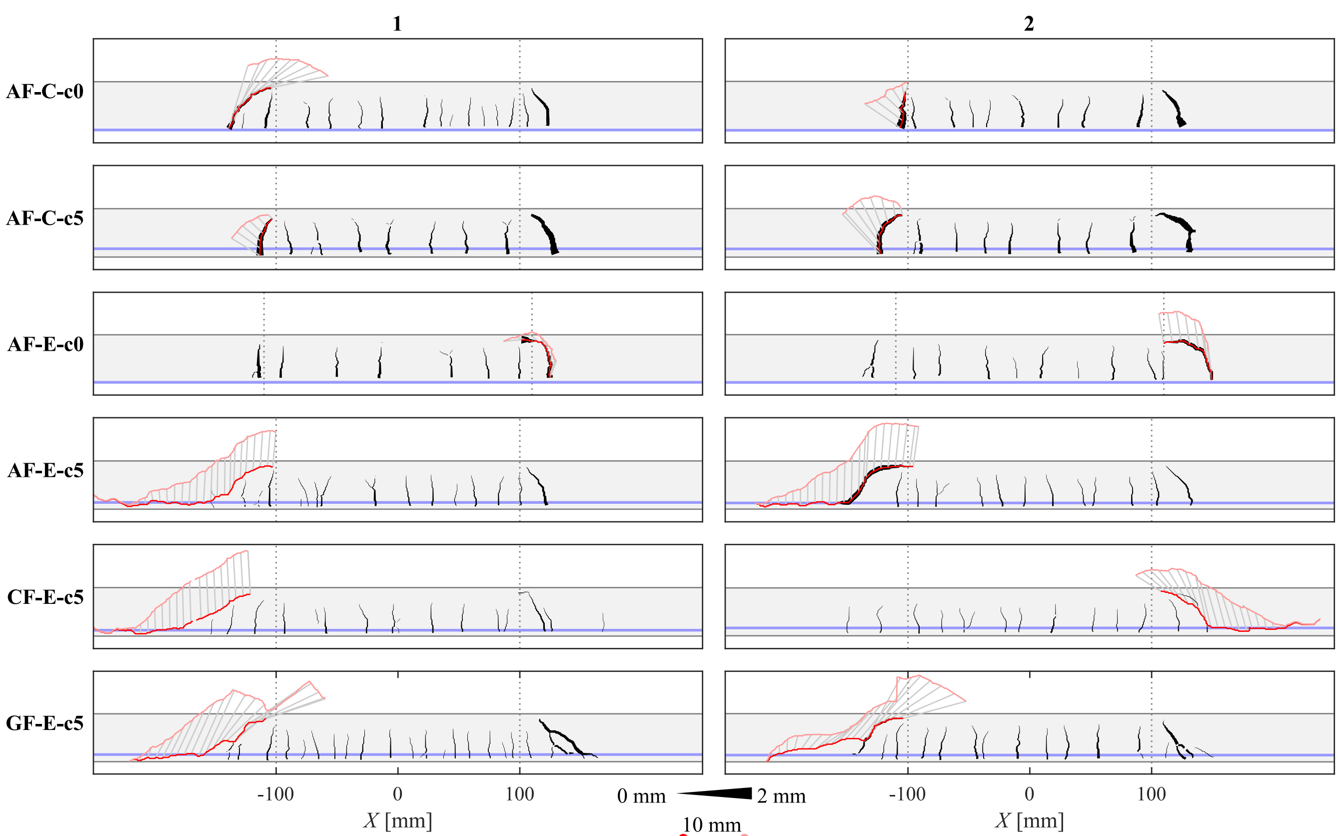

Fig. 10. Crack patterns right before failure (in black, with the line thickness corresponding to crack width) and failure crack in (red with opening displacement vector in grey and rose lines). (For interpretation of the references to colour in this figure legend, the reader is referred to the web version of this article.)

Section 5.3.

All specimens with cement paste coating displayed a pronounced decrease in stiffness close to the ultimate load in the moment-deflection relationship, whereas most epoxy-coated specimens showed a fairly linear behaviour until failure. Only a few specimens with epoxy coating (e.g. 'AF-E-c5-2′ or 'GF-E-c5-2′) also exhibited a slight reduction of post-cracking stiffness. However, this phenomenon is not as clearly visible in the textile stress–strain relationship, where the curve mostly stays linear even close to failure (with only 'AF-C-c5-2′ showing some slight decrease). In these cases, the substantial increases of the deflections were caused by concentrated deformations in a single crack outside the constant moment zone, which eventually led to failure, as addressed in more detail in Sections 5.2 and 5.3.

5.2. Crack kinematics

The crack width measurements are based on the results from ACDM and were determined at the depth of the reinforcement using the crack opening planes obtained from linear regression, as described in Section 2 and shown in Fig. 7. The textile stress-crack width relationship in Fig. 8c considers the average of all opened cracks (crack opening at the depth of the reinforcement larger than 0.02 mm) within the constant moment zone. Most cracks usually formed in the initial cracking phase after reaching the tensile strength of the concrete. With increasing textile stresses in the post-cracking hardening phase, the average crack width increased fairly linearly, as can be seen for Specimen 'AF-C-c5-1′ in Fig. 9.

In some specimens, new major cracks still formed within the constant moment zone at higher loads, each of them causing a sudden decrease in

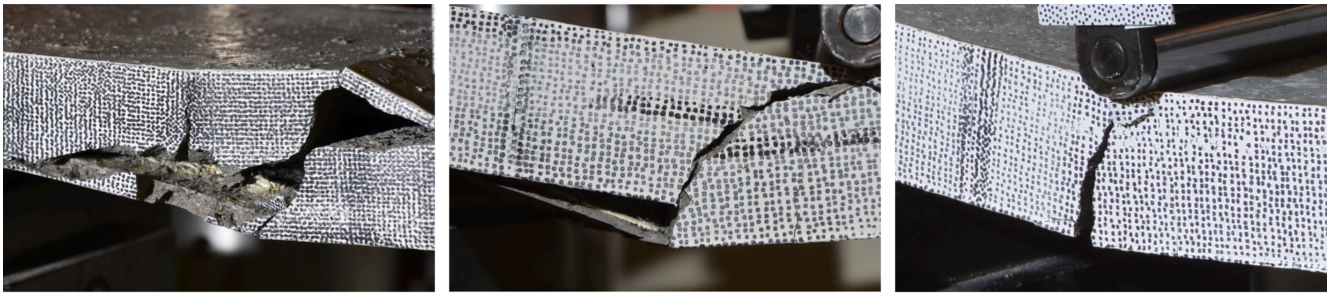

(a) (b) (c)

Fig. 11. Failure mechanisms: (a) bond ribs breaking out of concrete; (b) delamination of bottom-edge reinforcement; (c) bending-like failure in cement paste-coated specimens.

Table 4
Textile stresses at ultimate load, back-calculated bond shear stresses τ_b from uniaxial tension tests [20], and comparison of the measured average crack width and spacing with the predictions according to the Tension Chord Model.

Specimen	σ_{tu} [MPa]	σ_{tu}/f_{rov} [–]	τ_b [MPa]	at 0.5 × σ_{tu}: $w_{r,meas}$ [mm]	at 0.5 × σ_{tu}: $w_{r,TCM}$ [mm]	at 1.0 × σ_{tu}: $w_{r,meas}$ [mm]	at 1.0 × σ_{tu}: $w_{r,TCM}$ [mm]	$s_{r,meas}$ [mm]	$s_{r,TCM}$ [mm]
AF-C-c0	1579	0.75	2.5	0.14	0.10–0.20	0.23	0.32–0.65	18.8	28.8–57.6
	1614	0.77		0.20	0.10–0.21	0.36	0.34–0.67	27.6	29.2–58.3
AF-C-c5	1806	0.86		0.17	0.06–0.12	0.39	0.21–0.43	31.0	17.2–34.4
	1813	0.86		0.19	0.06–0.12	0.41	0.21–0.43	30.8	17.2–34.3
AF-E-c0	2459	0.95	2.0	0.25	0.24–0.48	0.66	0.59–1.18	37.9	32.0–64.0
	1348	0.52		0.15	0.08–0.16	0.27	0.27–0.55	28.1	32.2–64.3
AF-E-c5	1542	0.60		0.09	0.04–0.09	0.21	0.18–0.37	20.7	20.5–41.0
	1502	0.58		0.09	0.04–0.08	0.21	0.18–0.35	22.8	20.1–40.2
CF-E-c5	2329	0.63	1.3	0.09	0.07–0.14	0.18	0.23–0.47	23.1	31.2–62.3
	2014	0.55		0.07	0.05–0.10	0.14	0.19–0.39	21.8	32.4–64.8
GF-E-c5	1310	0.67	1.9	0.07	0.06–0.11	0.16	0.25–0.50	14.9	21.5–43.1
	1502	0.77		0.13	0.08–0.17	0.28	0.31–0.62	21.9	21.5–43.0

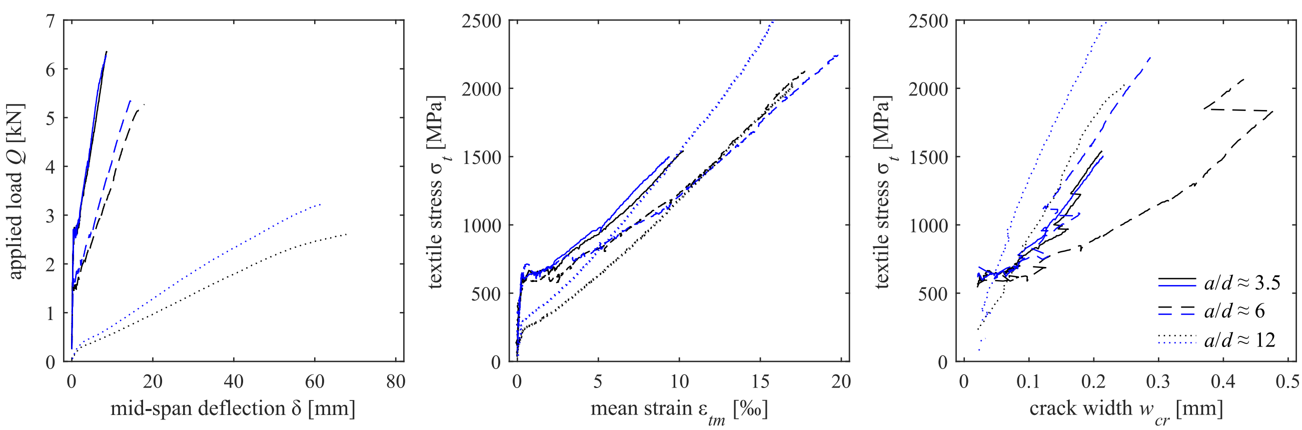

(a) (b) (c)

Fig. 12. Flexural response of beams with various shear slenderness.

the average crack width (e.g. 'AF-E-c0-2′). Specimen 'AF-E-c0-1′, which had to be re-loaded, was already initially cracked and no new cracks formed during the second loading cycle. The specimens where the cracking had stabilised earlier generally exhibited less variation in the crack widths. Nevertheless, the average crack widths of all specimens were in a plausible range compared to the uniaxial tension tests.

The average crack spacing (Fig. 8d) was determined by dividing the average crack width (w_r) by the mean strains (ε_{tm}). These graphs show the consecutive formation of cracks as a stepped function and are a good indicator of whether cracking has stabilised (i.e. no new cracks form within the constant moment zone, and the average crack spacing stays constant). The crack spacing determined in this way generally shows good agreement with the average crack spacing obtained by dividing the length of the constant moment zone by the number of cracks shortly before failure (denoted as faded lines in the $s_r - \varepsilon_{tm}$ relationships). The slight deviation may be caused by the scatter in the crack widths (e.g. due to finer cracks that form only close to failure or due to crack branching).

Fig. 10 shows the crack patterns close to ultimate load for all bending beams with the line thickness proportional to the crack opening. The cracks were generally evenly distributed within the constant moment zone. The crack spacings were fairly similar for all specimens (as shown in Fig. 8d), and the differences in crack spacing between specimens of the same configuration were also clearly visible in the crack widths (finer cracks at closer spacing). The specimens with concrete cover generally displayed smaller crack widths at the same stress level compared to the specimens with the bottom-edge reinforcement (‘AF-C-c0-1′ as the only exception), which is in line with the observation of a smaller tension stiffening effect in the latter, as described in Section 5.1.

5.3. Failure modes

Fig. 10 shows the contour of the critical crack that eventually led to failure in red colour. The displacement vectors of the measuring points are displayed as grey and rose lines. The specimens generally exhibited two different types of failure. All epoxy-coated specimens and one of the beams with cement-coated bottom-edge reinforcement (‘AF-C-c0-1′) failed in shear with a fairly vertical displacement in the critical crack. In most cases, the reinforcement delaminated along a horizontal crack branch with the bond ribs breaking out of the concrete (see Fig. 11a). For the specimens with bottom-edge reinforcement, this phenomenon is not directly visible in the crack displacement vectors since the DIC measurements could not track the displacement at the level of the reinforcement. However, the delamination crack is clearly visible in the broken specimens after failure, as shown in Fig. 11b. This type of shear crack failure occurred in a brittle manner without any prior announcement, except in Specimens ‘AF-E-c0-1′ and ‘AF-E-c5-2′, where the critical crack widened substantially before the eventual collapse. In the case of Specimen ‘GF-E-c5-1′, a shear crack appeared in the right shear span, which is also noticeable in the moment-deflection relationship as a slight drop in the applied load. However, the reinforcement did not delaminate in the right shear span, preventing the collapse mechanism and allowing the further increase of loading until the critical shear crack eventually occurred in the left shear span.

All cement-paste coated specimens expect ‘AF-C-c0-1′ showed a more bending-like failure (see Fig. 11c): the failure cracks displayed a fairly linear opening at ultimate load, and no delamination of the reinforcement occurred. The higher bond shear stresses for cement paste-coated textiles as observed in the corresponding uniaxial tension tests assured a better connection and less tendency for delamination of the reinforcement from the surrounding concrete. The failures occurred in the crack just outside the constant moment zone. The deformations concentrated in these cracks near the ultimate load, which explains the flattening of the moment-deflection curve (Fig. 8a) despite that the mean strains in the constant moment zone kept increasing fairly linearly. The textile stresses at ultimate load were slightly lower than in the corresponding uniaxial tension tests. The failure cracks did not open orthogonally but displayed some slip in the displacement vector, which indicates that the failure was not in pure bending. The visual inspection of the specimens after failure revealed that not all filaments within the rovings were ruptured and that the failure cracks had propagated into the compression zone, which might have caused the slip in the bending crack.

The substantially higher utilisation of the fibres compared to the roving strength of the pre-cracked specimen ‘AF-E-c0-1′ stands out when compared to all other specimens, and particularly to its twin ‘AF-E-c0-2′. Fig. 9 shows the utilisation of the textile reinforcement (textile stresses σ_t divided by the roving strength f_{rov}) against the crack opening of cracks, where the governing failure crack is displayed as a red line (the circle denoting the peak load). The specimens ‘AF-C-c5-1′ and ‘AF-E-c0-1′, which had a high utilisation, displayed stabilised cracking at an early stage of the load-deformation curve (note that ‘AF-E-c0-1′ was pre-cracked from the first loading phase), with no further cracks forming close to failure. Therefore, the bending cracks opened more evenly and uniformly. In both cases, two major cracks with wider openings formed just outside the constant moment zone (blue and red lines in Fig. 9), with one of them eventually leading to failure. The specimens ‘AF-E-c0-2′ and ‘GF-E-c5-1′, which are representative for most of the specimens that failed in shear, formed several further bending cracks in the hardening phase, leading to more scatter in the distributions of crack widths. In the case of ‘AF-E-c0-2′, the deformations eventually concentrated in one governing crack, failing in shear. As described in the previous section, the specimen ‘GF-E-c5-1′ displayed a substantial opening of an alleged shear crack. However, the failure occurred in the other span without any prior indication of an opening crack.

While shear cracks just outside the constant moment zone triggered failure, a collapse mechanism could only form once the reinforcement started delaminating from the concrete. The observed behaviour shows that the progressive opening of parallel cracks with similar crack widths decreases the tendency of deformations localising in one single crack and delays the debonding of the textile, which eventually leads to failure. This could be explained by the fact that larger crack widths generally lead to larger slip between reinforcement and concrete, while as – known from typical bond-slip relationships for conventional textile reinforcement (e.g. [12,41,42]) – the bond shear stresses decrease with increasing slip after reaching the peak value (typically between 0.05 and 0.5 mm, depending on the type of roving and coating). However, more refined experiments and analyses of the stress transfer and the bond conditions between textile and reinforcement are needed to corroborate this observation.

The observations and findings on the failure modes revealed several challenges regarding the shear capacity of weft-knitted textile reinforced concrete slabs. The formation of a delamination crack along the reinforcement, eventually leading to failure, has also been reported in studies with conventional textile reinforcement (e.g. [43–45]). Weft-knitted textiles are more prone to this type of failure due to their closed surface, which prevents the concrete from flowing through the reinforcement layer. Therefore, the influence of the bond ribs and the potential optimisation of their geometry to enhance the mechanical interlock between the reinforcement and the concrete needs to be investigated in future research. Furthermore, the use of a fine-grained concrete (i.e. $D_{max} = 2$ mm) leads to a low contribution from aggregate interlock, which is highly dependent on the maximum aggregate size. Although few studies exist on the shear strength of conventional textile reinforced concrete members (e.g. [46,47]), there are still no mechanically consistent models nor standardised design codes, which may allow the estimation of the shear capacity of weft-knitted textile reinforced concrete slabs. The influence of the specimen geometry (i.e. cross-section height and span) and the reinforcement ratio on the flexural behaviour and the resulting failure mode will be described in more detail in Section 5.5.

5.4. Prediction of the load-deformation behaviour with the Tension Chord Model

The behaviour of the tension chord of the beams is estimated with the approach presented in Section 3. The strain difference $\Delta\varepsilon$ given by Equation (1) allows the prediction of the stress–strain relationship in the tension chord of the bending beam, which is represented as a grey area in Fig. 8b (with the ratio of the possible crack spacings to the maximum crack spacing lying anywhere between 0.5 and 1). The predictions account for the equivalent reinforcement ratio of the specimens with concrete cover and the textile stiffness from the roving tests. Therefore, the predicted behaviour does not directly apply to the corresponding uniaxial tensile tests and the specimens with bottom-edge reinforcement due to their slightly different reinforcement ratio. The estimations from the TCM generally show good agreement with the experimental results. The tension stiffening effect ($\Delta\varepsilon$) gets slightly underestimated for the specimens with glass fibre inlays, which may be caused by the slightly lower textile stiffness obtained from the roving tests compared to the textile-concrete composites as stated in [20].

The estimations of the crack width and the crack spacing according to Eqs. (5) and (6) are summarised in Table 4. The bond shear stresses were back-calculated from the corresponding uniaxial tension tests assuming a constant bond shear stress-slip relationship and are included in Table 4. While all aramid specimens generally compared well with the TCM, the results from the specimens with carbon and glass fibre rovings displayed rather larger deviations from the model predictions with increasing load, especially regarding the average crack spacing and width. The crack widths at ultimate load (i.e. $1.0 \times \sigma_{tu}$) were overestimated. In the case of the specimens with glass fibre inlays ('GF-E-c5′'), the slightly stiffer behaviour of the tension chord compared to the stiffness obtained from the roving tests, as shown in Fig. 8b, led to larger estimations of the crack widths following Equation (6). Furthermore, the textile stress-crack width relationship (Fig. 8c) shows that few new cracks had formed at higher load levels in the specimens with carbon fibre inlays ('CF-E-c5′') and Specimen 'GF-E-c5-1′', which led to a reduction of the average crack spacing, explaining the good agreement at lower load levels but larger difference at ultimate load. Following Equation (5), the crack spacing is essentially dependent on the bond shear stresses, which were back-calculated from the results of the uniaxial tension tests, presented in [20], where only two specimens were tested per configuration. However, the observed and predicted relationship between crack width and spacing (since $w_r \approx s_r \cdot \varepsilon_{tm}$, when neglecting the elastic concrete strains in tension) still exhibited good agreement. Therefore, more experiments specifically targeting the bond behaviour (e.g. pull-out tests) may be the subject of future research to achieve a more reliable prediction of the crack spacing, which will eventually improve the crack width estimation.

5.5. Effect of shear slenderness

To eventually reach a bending failure, the shear slenderness of two pairs of specimens with the same reinforcement type (aramid fibres with epoxy coating) and amount was stepwise increased. The increase of the shear slenderness (a/d) from 3.5 to 6 was reached by increasing the spans and shifting the location of the applied loads (while the cross-section height remained the same). To achieve a shear slenderness of 12, the specimen height was reduced to only 12 mm. The intermediate shear slenderness ($a/d = 6$) still resulted in a shear failure, although the textiles reached a much higher utilisation, being close to the tensile strength of the roving. The two specimens with a cross-section height of only 12 mm and bottom-edge reinforcement eventually failed in bending. However, the deflections at ultimate load were substantially higher due to the low depth of the cross-section, which may limit the full utilisation of the tensile capacity of the reinforcement in structural applications due to the serviceability requirements becoming governing for the design.

The load–displacement relationship of the three configurations does not allow a direct comparison of the mechanical behaviour of the textile reinforcement beyond a qualitative description (see Fig. 12a). In contrast, the stress–strain relationship (Fig. 12b), which was obtained using the procedure presented in Section 2, reveals the similar behaviour of the reinforcement in all beams, proving the applicability of the material properties to various geometries. The cracking behaviour (Fig. 12c) is also quite similar for most specimens. The larger crack widths in one of the specimens probably resulted from the narrow constant moment zone due to the shift of the load introduction towards the middle of the beam. Only few cracks formed in the constant moment zone, and thus, the measurement of the average crack width is more sensitive to local variations and outliers, as shown in Fig. 12c, where the formation of a new crack close to failure led to a distinct drop in the average crack width. Therefore, an adequate choice of geometry, specifically the length of the constant moment zone in relation to the crack spacing, is needed for the procedure to robustly capture the behaviour in pure bending.

6. Conclusions

This study examined the flexural response of concrete beams with weft-knitted textile reinforcement. The experimental campaign consisted of four-point-bending tests, varying the fibre materials (aramid, carbon or glass fibres), the coating types (cement paste or epoxy resin), and the location of the reinforcement (with concrete cover or as bottom-edge reinforcement). Based on the results from the digital image correlation measurements and the 'Automated Crack Detection and Measurement' tool, a methodology for the analysis of the behaviour of the tension chord within the constant moment zone was presented, which enables a direct comparison of bending tests with different geometries and reinforcement contents. The methodology consists in extracting the mean strains through a regression analysis of the horizontal displacements over the cross-section and a thorough consideration of the crack geometry and kinematics within the constant moment zone. This yields information about average deformations, crack spacings and crack widths of the reinforcement. While the approach is applicable to any kind of reinforcement, it is particularly suitable for textile reinforcement in which the average deformations within a roving cannot be directly measured due to the inhomogeneous stress distribution within the roving cross-section. The Tension Chord Model, which had proved to adequately capture the mechanical behaviour of tension ties with weft-knitted textile reinforcement, was applied to the bending beams, following the approach proposed by Marti [34] and Burns [35] for the estimation of the effective concrete area activated in tension.

The analysis of the tension chord yielded a good correlation of the weft-knitted textile reinforced concrete beams with the corresponding direct tension tests regarding the stress–strain relationship and the crack kinematics, generally confirming the fundamental findings from the previous study on the uniaxial tensile response. Therefore, the proposed methodology to evaluate the behaviour of the tension chord in bending tests proved to be a reliable alternative to direct tension tests, which significantly simplifies the comparison of different geometries, materials and reinforcement contents, also allowing to study the effect of tension stiffening in bending and the shear failures, which are not possible if only the load–deflection data is provided.

The general load-deformation behaviour of the bending beams with weft-knitted textile reinforcement was characterised by stable multiple cracking and a hardening phase after exceeding the tensile strength of the concrete, which is similar to conventional woven textile reinforcement. The specimens with epoxy coating prematurely failed in shear with a distinct delamination crack along the interface of reinforcement and concrete. Most of the cement paste-coated specimens exhibited a more bending-like failure with a fairly linear opening of a steep failure crack just outside the constant moment zone, although the rovings did not fully rupture and some slip was still visible in the crack displacement due to the propagation of the crack into the compression zone. Therefore, the utilisation of the reinforcement in terms of textile stresses at ultimate load was generally lower than in the uniaxial tensile tests and cannot be considered as representative for the full bending capacity. The specimens with bottom-edge reinforcement generally displayed the same behaviour as their counterparts with concrete cover but with a lesser tension stiffening effect due to the smaller effective concrete area, leading to larger crack widths. The results from the ACDM tool revealed a beneficial post-cracking behaviour for all specimens with narrow cracks at a small, even spacing, which were in a similar range as in the specimens in uniaxial tension. The calculation of the crack spacing based on the mean strains and the average crack width proved to be a reliable indicator for the crack formation, which showed that major cracks could still form in the hardening phase, although most specimens achieved crack stabilisation already at lower load levels.

The stress–strain relationship of most specimens could be predicted well using the TCM; note that only few parameters need to be known, and that they were determined a priori in separate material tests. Only in the case of the glass fibre inlays, the experimental results exhibited a slightly higher tension stiffening effect than expected, which might have been caused by an underestimation of the textile stiffness, as also observed in the study of the uniaxial tension tests [20]. The estimations of the crack widths and crack spacings displayed a good correlation for the specimens with aramid inlays, but larger differences for carbon and glass fibres. The bond shear stresses used for these predictions were back-calculated from the uniaxial tension tests and exhibited rather large scatter, which emphasises the need for more elaborate tests, particularly targeting the capture of the bond shear stress-slip relationship, e.g. pull-out tests.

The objectives of this study were to verify the applicability of weft-knitted textile reinforcement for concrete beams in bending. Thereby, the proposed evaluation methodology to assess the mechanical response in the tension chord allowed the direct comparison with uniaxial tension tests with the same type of reinforcement, and may be used in future research for the analysis and comparison of conventional textile reinforcement or other types of concrete composites. The experimental results show that the general behaviour of this new type of reinforcement and its interaction with concrete, which had been studied earlier in uniaxial tension tests, are well applicable to bending beams. The placement of the reinforcement at the bottom edge of the specimens led to similar results as the corresponding bending beams with concrete cover, which opens up the feasibility of the use of the textile as stay-in-place formwork with the integrated function as reinforcement in the final state of the structure. The knitting technology offers many possibilities, such as integrating inlays in both warp and weft direction or introducing other spatial features beyond bond ribs such as shear connectors to prevent premature failure due to delamination of the reinforcement from the concrete. While the geometric flexibility of the textiles allows for more complex structures (such as doubly curved shells or folded plates), the increased complexity and superposition of various loading conditions (such as bi-axial membrane forces and bending, or in-plane shear) need to be investigated in further research to fully exploit these possibilities.

CRediT authorship contribution statement

Minu Lee: Conceptualization, Methodology, Investigation, Visualization, Writing – original draft. **Jaime Mata-Falcón:** Conceptualization, Methodology, Writing – review & editing, Supervision. **Walter Kaufmann:** Conceptualization, Writing – review & editing, Funding acquisition.

Declaration of Competing Interest

The authors declare that they have no known competing financial interests or personal relationships that could have appeared to influence the work reported in this paper.

Acknowledgements

The authors gratefully acknowledge Dr. Mariana Popescu from Block Research Group (ETHZ) and Dr. Lex Reiter from the Chair of Physical Chemistry of Building Materials (ETHZ) for contributing their technical and practical expertise, as well as the students Nathalie Chiaverio, Salome Geiser and Caterina Rovati for their valuable support during preparation and testing of the specimens. This research is supported by the National Centre for Competence in Research in Digital Fabrication, funded by the Swiss National Science Foundation (project number 51NF40-141853).

Open access data

The experimental data presented in this article was submitted to a public data repository and is published under the following https://doi.org/10.3929/ethz-b-000520292.

Appendix A

A.1. Bending moment and normal force at cracking in a beam and a tension tie, respectively

$$M_{cr} = f_{ct,fl} \cdot \frac{h^2 \cdot b}{6} = \sigma_{tr} \cdot A_t \cdot \left(d - \frac{x}{3}\right)$$

$$N_{cr} = f_{ct} \cdot A_c + f_{ct} \cdot \left(\frac{E_t}{E_c} - 1\right) \cdot A_c = \sigma_{tr} \cdot A_t$$

A.2. Cross-section analysis for cracked reinforced concrete

$$EI^{II} = A_t \cdot E_t \cdot (d - x) \cdot \left(d - \frac{x}{3}\right)$$

$$x = d \cdot \left(\sqrt{n^2 \cdot \rho^2 + 2 \cdot \rho \cdot n} - n \cdot \rho\right) \text{ with } \rho = \tfrac{A_t}{b \cdot d},\ n = \tfrac{E_t}{E_c}.$$

A.3. Derivation of crack spacing and crack width

$$(\sigma_c + d\sigma_c) \cdot a_c = \sigma_c \cdot a_c + n_b \cdot \tau_b \cdot dx \rightarrow \tfrac{d\sigma_c}{dx} = \tfrac{n_b \cdot \tau_b}{a_c} = \tfrac{n_b \cdot \tau_b \cdot \rho}{(1-\rho) \cdot a_t}$$

$$s_{r0} = 2 \cdot \frac{f_{ct}}{d\sigma_c / dx} = 2 \cdot f_{ct} \cdot \left(\frac{(1-\rho) \cdot a_t}{n_b \cdot \tau_b \cdot \rho}\right)^{-1}$$

$$\varepsilon_{tm} = \frac{\sigma_{tr}}{E_t} - \Delta\varepsilon = \frac{\sigma_{tr}}{E_t} - \frac{\lambda \cdot f_{ct} \cdot (1-\rho)}{2 \cdot \rho \cdot E_t}$$

$$\varepsilon_{cm} = \frac{\lambda \cdot f_{ct}}{E_c} = \frac{\lambda \cdot f_{ct} \cdot n_t}{E_t}$$

$$w_r = s_r \cdot (\varepsilon_{tm} - \varepsilon_{cm}) = \lambda \cdot s_{r0} \cdot \left(\frac{\sigma_{tr}}{E_t} - \frac{\lambda \cdot f_{ct} \cdot (1-\rho)}{2 \cdot \rho \cdot E_t} - \frac{\lambda \cdot f_{ct} \cdot n_t}{E_t}\right) = \frac{\lambda \cdot s_{r0}}{2 \cdot E_t} \cdot \left(2 \cdot \sigma_{tr} - \lambda \cdot \underbrace{f_{ct} \cdot \left(\frac{1}{\rho} + n - 1\right)}_{\sigma_{tr0}}\right)$$

A.4. Correlation coefficient of crack openings from measurements and linear regression

See Fig. 13.

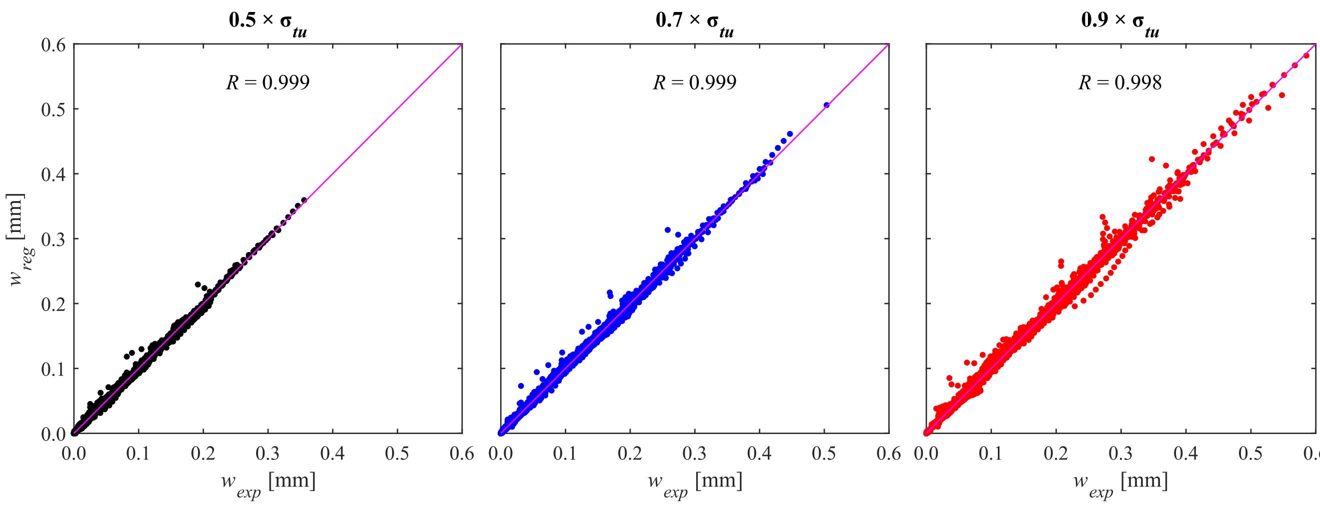

Fig. 13. Correlation of crack openings from direct measurements on the basis of digital image correlation and linear regression of all specimens.

References

[1] Curbach M, Jesse F. Eigenschaften und Anwendung von Textilbeton. BUST 2009; 104(1):9–16.

[2] Hegger J, Kulas C, Schneider HN, Brameshuber W, Hinzen M, Raupach M, et al. TRC pedestrian bridge - design, load-bearing behavior and production processes of a slender and lightweight construction. In: Brameshuber W, editor. Aachen: RILEM Publications SARL; 2010.

[3] Hegger J, Curbach M, Stark A, Wilhelm S, Farwig K. Innovative design concepts: Application of textile reinforced concrete to shell structures. Struct Concr 2018;19: 637–46. https://doi.org/10.1002/suco.201700157.

[4] Brückner A, Ortlepp R, Curbach M. Textile reinforced concrete for strengthening in bending and shear. Mater Struct 2006;39:741–8. https://doi.org/10.1617/s11527-005-9027-2.

[5] Mechtcherine V. Novel cement-based composites for the strengthening and repair of concrete structures. Constr Build Mater 2013;41:365–73. https://doi.org/10.1016/j.conbuildmat.2012.11.117.

[6] Frenzel M. Bemessung texilbetonverstärkter Stahlbetonbauteile unter Biegebeanspruchung. Beton- Stahlbetonbau 2015;110:54–68. https://doi.org/10.1002/best.201400115.

[7] Peled A, Mobasher B, Bentur A. Textile Reinforced Concrete. Boca Raton, FL: CRC Press, Taylor & Francis Group; 2017.

[8] Curbach M, editor. Sachstandbericht zum Einsatz von Textilien im Massivbau. Berlin: Beuth; 1998.

[9] Hegger J, Horstmann M, Voss S, Will N. Textilbewehrter Beton: Tragverhalten, Bemessung und Anwendung. Beton- Stahlbetonbau 2007;102:362–70. https://doi.org/10.1002/best.200700552.

[10] Mader E, Plonka R, Schiekel M, Hempel R. Coatings on alkali-resistant glass fibres for the improvement of concrete. J Ind Text 2004;33:191–207. https://doi.org/10.1177/1528083704039833.

[11] Quadflieg T, Leimbrink S, Gries T, Stolyarov O. Effect of coating type on the mechanical performance of warp-knitted fabrics and cement-based composites. J Compos Mater 2018;52:2563–76. https://doi.org/10.1177/0021998317750003.

[12] Fernàndez Ruiz M, Muttoni A. Building in a lighter and more sustainable manner: textile reinforced concrete for thin structural elements. cemsuisse 2017.

[13] Valeri P, Fernàndez Ruiz M, Muttoni A. Tensile response of textile reinforced concrete. Constr Build Mater 2020;258:119517. https://doi.org/10.1016/j.conbuildmat.2020.119517.

[14] Glowania M, Gries T, Schoene J, Schleser M, Reisgen U. Innovative coating technology for textile reinforcements of concrete applications. KEM 2011;466: 167–73. https://doi.org/10.4028/www.scientific.net/kem.466.167.

[15] Popescu M, Rippmann M, Van Mele T, Block P. Automated generation of knit patterns for non-developable surfaces. In: De Rycke K, Gengnagel C, Baverel O, Burry J, Mueller C, Nguyen MM, Rahm P, Thomsen MR, editors. Humanizing digital reality. Singapore: Springer Singapore; 2018. p. 271–84.

[16] Popescu M, Reiter L, Liew A, Van Mele T, Flatt RJ, Block P. Building in Concrete with an Ultra-lightweight Knitted Stay-in-place Formwork: Prototype of a Concrete Shell Bridge. Structures 2018;14:322–32. https://doi.org/10.1016/j.istruc.2018.03.001.

[17] Popescu M, Rippmann M, Liew A, Reiter L, Flatt RJ, Van Mele T, et al. Structural design, digital fabrication and construction of the cable-net and knitted formwork of the KnitCandela concrete shell. Structures 2021;31:1287–99.

[18] Popescu M, Rippmann M, Liew A, Van Mele T, Block P. Concrete shell built using a knitted formwork. DETAIL Struct 2019;1:10–1.

[19] Lee M, Mata-Falcón J, Popescu M, Block P, Kaufmann W. Potential approaches for reinforcing complex concrete structures with integrated flexible formwork. In: Second RILEM International Conference on Concrete and Digital Fabrication, vol. 28; 2020. p. 669–79. https://doi.org/10.1007/978-3-030-49916-7_67.

[20] Lee M, Mata-Falcón J, Kaufmann W. Load-deformation behaviour of weft-knitted textile reinforced concrete in uniaxial tension. Mater Struct 2021;54:210. https://doi.org/10.1617/s11527-021-01797-5.

[21] RILEM Technical Committee 232-TDT (Wolfgang Brameshuber). Recommendation of RILEM TC 232-TDT: test methods and design of textile reinforced concrete. Mater Struct 2016;49:4923–7. https://doi.org/10.1617/s11527-016-0839-z.

[22] Mata-Falcón J, Haefliger S, Lee M, Galkovski T, Gehri N. Combined application of distributed fibre optical and digital image correlation measurements to structural concrete experiments. Eng Struct 2020;225:111309. https://doi.org/10.1016/j.engstruct.2020.111309.

[23] Marti P, Alvarez M, Kaufmann W, Sigrist V. Tension Chord Model for Structural Concrete. Struct Eng Int 1998;8:287–98. https://doi.org/10.2749/101686698780488875.

[24] Peled A, Bentur A, Yankelevsky D. Flexural Performance of Cementitious Composites Reinforced with Woven Fabrics. J Mater Civ Eng 1999;11:325–30. https://doi.org/10.1061/(ASCE)0899-1561(1999)11:4(325).

[25] Williams Portal N, Nyholm Thrane L, Lundgren K. Flexural behaviour of textile reinforced concrete composites: experimental and numerical evaluation. Mater Struct 2017;50:4. https://doi.org/10.1617/s11527-016-0882-9.

[26] Hawkins W, Orr J, Ibell T, Shepherd P. An Analytical Failure Envelope for the Design of Textile Reinforced Concrete Shells. Structures 2018;15:56–65. https://doi.org/10.1016/j.istruc.2018.06.001.

[27] Yu Q, Valeri P, Fernández Ruiz M, Muttoni A. A consistent safety format and design approach for brittle systems and application to textile reinforced concrete structures. Eng Struct 2021;249:113306. https://doi.org/10.1016/j.engstruct.2021.113306.

[28] Gehri N, Mata-Falcón J, Kaufmann W. Automated crack detection and measurement based on digital image correlation. Constr Build Mater 2020;256: 119383. https://doi.org/10.1016/j.conbuildmat.2020.119383.

[29] Gehri N, Mata-Falcón J, Kaufmann W. Refined extraction of crack characteristics in Large-scale concrete experiments based on digital image correlation. Eng Struct 2022;251:113486. https://doi.org/10.1016/j.engstruct.2021.113486.

[30] Kuuskoski V. Über die Haftung zwischen Beton und Stahl. Doctoral Thesis. The State Institute for Technical Research; 1950.

[31] Rehm G. Über die Grundlagen des Verbundes zwischen Stahl und Beton 1961;vol. Heft 138:59.

[32] Borosnyói A, Balázs GL. Models for flexural cracking in concrete: the state of the art. Struct Concr 2005;6:53–62. https://doi.org/10.1680/stco.2005.6.2.53.

[33] Galkovski T, Mata-Falcón J, Kaufmann W. Effective reinforcement ratio of RC beams: Validation of modelling assumptions with high-resolution strain data. suco.202100739 Struct Concr 2022. https://doi.org/10.1002/suco.202100739.

[34] Marti P. Reinforced concrete i lecture notes. Department of Civil, Environmental and Geomatic Engineering, ETH Zurich; 2004.
[35] Burns C. Serviceability analysis of reinforced concrete based on the tension chord model. ETH Zürich 2012. https://doi.org/10.3929/ethz-a-009753066.
[36] International Federation for Structural Concrete. fib model code for concrete structures 2010. Berlin: Ernst & Sohn; 2013.
[37] R&G Faserverbundwerkstoffe GmbH. Technische Daten - Epoxydharz L; 2020.
[38] DIN EN 196-1:2016-11. Prüfverfahren für Zement_- Teil_1: Bestimmung der Festigkeit; Deutsche Fassung EN_196-1:2016. Beuth Verlag GmbH; 2016. https://doi.org/10.31030/2482416.
[39] Correlated Solutions. Vic-3D Software Manual. Correlated Solutions Inc.; 2019.
[40] Fachbereich Prozessmesstechnik und Strukturanalyse. VDI/VDE 2626 Blatt 1 - Optische Messverfahren - Bildkorrelationsverfahren - Grundlagen und Begriffe. VDI/VDE-Gesellschaft Mess- und Automatisierungstechnik; 2018.
[41] Banholzer B, Brockmann T, Brameshuber W. Material and bonding characteristics for dimensioning and modelling of textile reinforced concrete (TRC) elements. Mater Struct 2006;39:749–63. https://doi.org/10.1617/s11527-006-9140-x.
[42] Häußler-Combe U, Hartig J. Bond and failure mechanisms of textile reinforced concrete (TRC) under uniaxial tensile loading. Cem Concr Compos 2007;29:279–89. https://doi.org/10.1016/j.cemconcomp.2006.12.012.
[43] Du Y, Zhang X, Liu L, Zhou F, Zhu D, Pan W. Flexural Behaviour of Carbon Textile-Reinforced Concrete with Prestress and Steel Fibres. Polymers 2018;10:98. https://doi.org/10.3390/polym10010098.
[44] Kamani R, Kamali Dolatabadi M, AliAA J. Flexural design of textile-reinforced concrete (TRC) using warp-knitted fabric with improving fiber performance index (FPI). J Textile Inst 2018;109:492–500. https://doi.org/10.1080/00405000.2017.1356000.
[45] Rempel S, Ricker M, Hegger J. Biegebemessungsmodell mit einer geschlossenen und iterativen Lösung für Textilbetonbauteile. Beton- Stahlbetonbau 2020;115:218–30. https://doi.org/10.1002/best.201900086.
[46] Bielak J, Adam V, Hegger J, Classen M. Shear Capacity of Textile-Reinforced Concrete Slabs without Shear Reinforcement. Appl Sci 2019;9:1382. https://doi.org/10.3390/app9071382.
[47] Bielak J, Hegger J. Enhancing shear capacity of thin slabs with CFRP shear reinforcement: Experimental study. Struct Concr 2021;22:3057–73. https://doi.org/10.1002/suco.202100325.